Dual regulation of osteosarcoma hypoxia microenvironment by a bioinspired oxygen nanogenerator for precise single-laser synergistic photodynamic/photothermal/induced antitumor immunity therapy

Chongqing Zhang [a,b,1], Dongsheng Li [c,1], Xin Zhang [b,1], Rong Dai [c], Weiwei Kang [c], Yao Li [c], Qin Liu [c], Mengting Gao [c], Ziliang Zheng [c,**], Ruiping Zhang [c,*], Zhaohui Wen [a,***]

[a] Department of Neurology, Brain Ultrasound, First Affiliated Hospital of Harbin Medical University, Harbin, 150001, Heilongjiang Province, China
[b] Medical Imaging Department, Shanxi Province Cancer Hospital (Shanxi Hospital Affiliated to Cancer Hospital, Chinese Academy of Medical Sciences/Cancer Hospital Affiliated to Shanxi Medical University), Taiyuan, 030001, China
[c] Department of Radiology, Fifth Hospital of Shanxi Medical University (Shanxi Provincial People's Hospital), Taiyuan, 030000, China

A R T I C L E   I N F O

A B S T R A C T

The hypoxic tumor microenvironment (TME) of osteosarcoma (OS) is the Achilles' heel of oxygen-dependent photodynamic therapy (PDT), and tremendous challenges are confronted to reverse the hypoxia. Herein, we proposed a "reducing expenditure of O_2 and broadening sources" dual-strategy and constructed ultrasmall IrO_2@BSA-ATO nanogenerators (NGs) for decreasing the O_2-consumption and elevating the O_2-supply simultaneously. As O_2 NGs, the intrinsic catalase (CAT) activity could precisely decompose the overexpressed H_2O_2 to produce O_2 in situ, enabling exogenous O_2 infusion. Moreover, the cell respiration inhibitor atovaquone (ATO) would be at the tumor sites, effectively inhibiting cell respiration and elevating oxygen content for endogenous O_2 conservation. As a result, IrO_2@BSA-ATO NGs systematically increase tumor oxygenation in dual ways and significantly enhance the antitumor efficacy of PDT. Moreover, the extraordinary photothermal conversion efficiency allows the implementation of precise photothermal therapy (PTT) under photoacoustic guidance. Upon a single laser irradiation, this synergistic PDT, PTT, and the following immunosuppression regulation performance of IrO_2@BSA-ATO NGs achieved a superior tumor cooperative eradicating capability both *in vitro* and *in vivo*. Taken together, this study proposes an innovative dual-strategy to address the serious hypoxia problem, and this microenvironment-regulable IrO_2@BSA-ATO NGs as a multifunctional theranostics platform shows great potential for OS therapy.

1. Introduction

Osteosarcoma (OS) is the most common malignant musculoskeletal tumor, which persists as a formidable menace to human well-being [1–3]. Despite advanced strategies including surgery, adjuvant chemotherapy, and radiation therapy, the prognosis of OS remains poor. Thus, it is still a challenge to develop an efficient treatment strategy for counteracting OS progression [4,5]. Phototherapy, especially photodynamic therapy (PDT), has aroused great interest in recent years owing to its unique advantages, which consist of minimal invasiveness,

unequivocal efficacy, and negligible toxicity [6]. This effective therapeutic approach, which harnesses the symbiosis of light and photosensitizers, has been used clinically to treat superficial diseases encompassing dermatologic lesions, retinal afflictions, and epithelial neoplasms [7–9]. The strategic irradiation of photosensitizers within the near-infrared (NIR) spectrum, specifically at 700 nm–1100 nm, unveils the ability to selectively illuminate the recesses of malignant tissues. This orchestrated illumination prompts the generation of reactive oxygen species (ROS), thus holding immense potential in surmounting the formidable hurdle posed by the limited depth during solid tumor

therapies [10].

The conventional paradigm of PDT hinges on the cytotoxic impact induced by a photosensitizer under the irradiation of light, which catalyzes the transformation of molecular oxygen (O_2) into reactive oxygen species (ROS) [11]. These ROS, in turn, orchestrate cellular demise and the ensuing destruction of the tumor cells. In addition, the inherent characteristic of O_2 consumption in conventional PDT renders its efficacy markedly contingent on the O_2 levels within the tissue. Regrettably, hypoxia, an intrinsic tumor microenvironment (TME) attribute of solid tumors including OS, stemming from the swift progression of aggressive cell proliferation and the aberrant formation of blood vessels, casts a pall over its effectiveness [12,13]. The continuous O_2 consumption inherent in PDT exacerbates hypoxia, thereby accentuating resistance to the therapy and circumscribing its efficiency [14]. Recognizing the pivotal role of hypoxia in OS advancement and its resistance to therapeutic interventions, concerted endeavors have been directed at surmounting the constraints posed by hypoxia in PDT. A prevailing strategy for augmenting intratumoral O_2 perfusion is the direct administration of O_2 [15,16]. Recently, carriers for transporting exogenous O_2 have been developed, including biocompatible red blood cells (RBCs), perfluorocarbons (PFCs), and fluorinated materials [17–19]. Nonetheless, these approaches offer only transient relief from hypoxia and bear the risk of relapse. Moreover, the inadvertent reoxygenation may inadvertently furnish tumor cells with an oxygen-rich milieu conducive to their proliferation, thus counteracting a portion of the anticipated positive outcomes [20]. Consequently, the pursuit of an effective approach capable of accurately enhancing OS oxygenation during PDT remains a subject of profound significance, albeit one fraught with formidable challenges.

It is well known that tumor cells manifest uncontrolled growth and have elevated metabolic requirements [21]. The mitochondrial oxidative phosphorylation process plays a pivotal role in the production of cellular energy by consuming O_2 [22,23]. In the realm of OS cells, inhibition of oxidative phosphorylation holds the promise of diminishing O_2 utilization and curtailing ATP synthesis. The O_2 content in tumor tissue pivots on the delicate equilibrium between the rate of O_2 supply via the vasculature and the Oxygen Consumption Rate (OCR) intrinsic to tumor tissues. Consequently, a promising strategy for sustained mitigation of hypoxia lies in the reduction of OCR, which is a substantive facet of conserving endogenous O_2. Atovaquone (ATO), an FDA-approved small molecule pharmaceutical, manifests the capability to curtail O_2 consumption by inhibiting oxidative phosphorylation, which can preserve O_2 for the highly efficient execution of PDT [24]. For instance, Fan et al. established NPs that encapsulate dual-drug photosensitizers (PSs) and ATO, so as to attenuate hypoxia-induced resistance to PDT [25]. Additionally, Ren et al. reported a strategic nanodrug delivery system (SHRN) loaded with the oxygen consumption inhibitor ATO to improve tumor tissue oxygenation [26]. However, the modulation process is limited by the dose and delivery effects, and as a result, it failed to sufficiently increase tumor oxygenation by relying solely on ATO. Given the heightened levels of hydrogen peroxide (H_2O_2) associated with aberrant tumor cells, there emerges the tantalizing prospect of harnessing the decomposition of H_2O_2 into O_2 for in situ accurate O_2 generation. The plausible realization of this involves catalase (CAT), facilitating the on-demand expansion of the exogenous O_2 method, which is a burgeoning strategy that proved superior to direct O_2 delivery [27]. Recently, several IrO_2-based nanoparticles have been reported as promising carriers and to function as a CAT-mimic to catalyze the decomposition of H_2O_2 in the TME to generate endogenous oxygen and alleviate the hypoxia of solid tumors [28–30]. Decomposing overexpressed H_2O_2 to O_2 in situ by CAT-mimicking nanozymes, characterized by their intrinsic specificity and passive targeting for abnormal regions, circumvents the premature release of O_2 during circulation [31]. Hence, there is an urgent need to improve awareness of hypoxia TME and craft nanoparticles that combine multiple O_2-enhancing strategies, thereby augmenting the efficacy of PDT.

In this study, we proposed an innovative dual-strategy of "reducing the expenditure of O_2 and broadening sources" as a robust methodology for systematically increasing tumor oxygenation of OS (Scheme 1). Embodied within this stratagem is the facile synthesis of bioinspired iridium-oxide nanogenerators (NGs), laden with the clinically sanctioned drug ATO, an ensemble referred to as IrO_2@BSA-ATO NGs. First, the commendable biocompatibility and sufficiently diminutive size of the NGs facilitate their diffusion against the conspicuous interstitial pressure, which allows for the convenient reversal of hypoxia in the profound recesses of the tumor, thereby maximizing the overall benefit
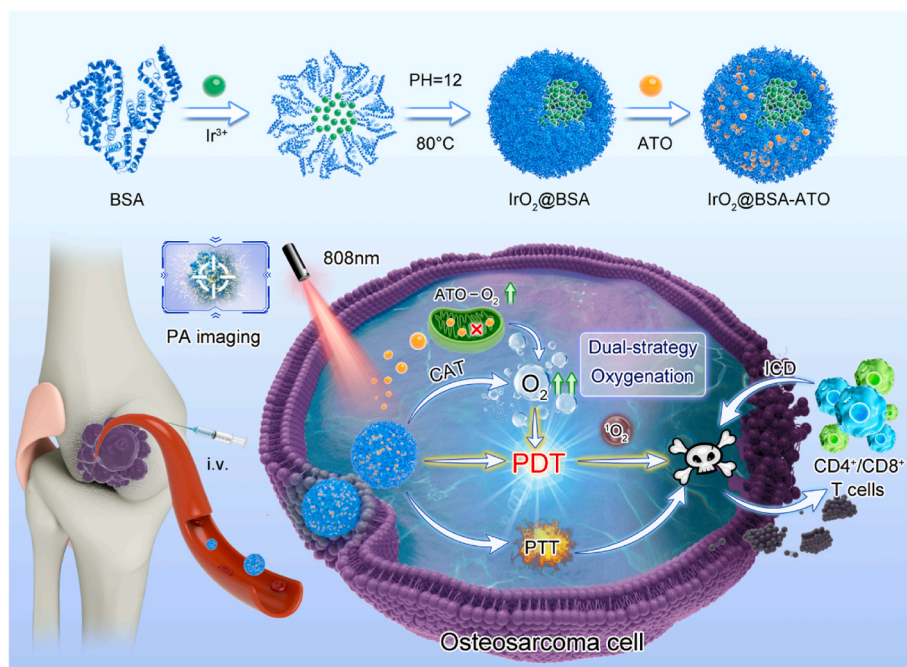

Scheme 1. **Scheme 1.** Schematic illustration of the IrO_2@BSA-ATO preparation, dual-strategy for increasing oxygenation to enhance PDT, and PA imaging-guided triple therapy.

derived from enhanced oxygenation. After being enriched in the tumor through passive targeting, the CAT-mimicking activity inherent in the NGs ensures the decomposition of endogenous H_2O_2 to produce O_2 (broadening sources), thus elevating the partial pressure of O_2 and relieving hypoxia. On the other hand, the inhibition of mitochondrial oxidative phosphorylation by the released ATO molecules resulted in reduced O_2 consumption in cellular metabolism (reducing expenditure). Moreover, distinguished by their exceptional photothermal conversion efficiency, IrO_2@BSA-ATO NGs emerge as potent photothermal agents, facilitating photoacoustic (PA) imaging-guided synergistic PTT for the targeted obliteration of tumors. The augmented PDT and synergistic PTT under a single laser could release tumor-associated antigens (TAAs) and promote tumor infiltration of antitumor T cells, alleviating the immunosuppressive milieu. Upon single NIR laser irradiation, the IrO_2@BSA-ATO NGs execute a dual oxygen elevation strategy, rescuing the tumor from hypoxia. Thus, coupled with PA imaging-guided triple-therapeutic of PDT/PTT/induced antitumor immunity therapy, the IrO_2@BSA-ATO NGs orchestrate an efficacious onslaught against tumor cells, positioning them as a promising candidate in the realm of OS theranostics.

2. Results and discussion

2.1. Characterization of the oxygen nanogenerators (NGs)

IrO_2@BSA-ATO NGs were synthesized via a facile bio-mineralization approach, where atovaquone (ATO) was incorporated to impede mitochondrial oxidative phosphorylation [32]. This synthesis, accomplished through a bioinspired method, harnesses bovine serum albumin (BSA) as a versatile template, thereby ensuring ease of production as well as commendable biocompatibility. NGs were characterized using a transmission electron microscope (TEM), and it was found that the prepared NGs presented a spherical morphology (Fig. 1A). The size distribution analysis showed that NGs ranged from 2.0 to 4.1 nm, with an average particle diameter of approximately **2.97** nm (the inset in Fig. 1A), implying the size of the prepared NGs was relatively uniform. A closer inspection through High-Resolution Transmission Electron Microscopy (HRTEM) unveiled the emergence of IrO_2 nanocrystals in BSA matrices, with lattice spacings of 0.226 nm (inset of Fig. 1B) aligning with the diffraction (200) planes of IrO_2 nanocrystals (Fig. 1B) [33]. As demonstrated by elemental mapping based on energy-dispersive X-ray spectroscopy (TEM-EDS), an even distribution of O, N, and Ir within the NGs exhibited the successful synthesis of IrO_2@BSA-ATO NGs (Fig. 1C). The hydrodynamic size and zeta potential of the NGs were measured by
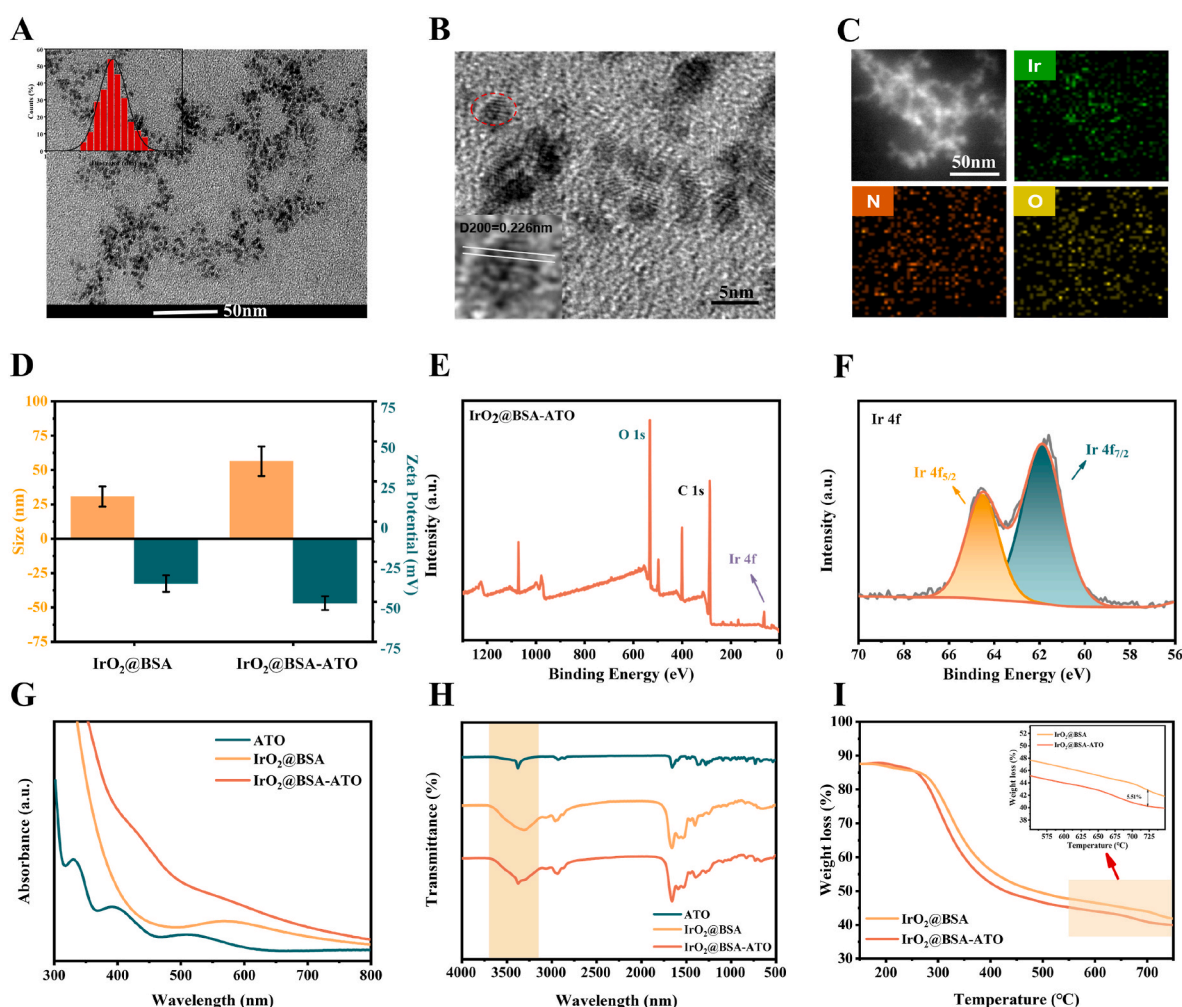

Fig. 1. Characterization of the oxygen nanogenerators (NGs). a) TEM image and size distribution (inset) of the IrO_2@BSA-ATO nanogenerators with ultrasmall particles. b) HRTEM image of IrO_2@BSA-ATO NGs. c) HAADF-STEM image and elemental mapping of IrO_2@BSA-ATO NGs. d) Hydrodynamic diameter and Zeta potential of IrO_2@BSA and IrO_2@BSA-ATO NGs. e) XPS spectra of IrO_2@BSA-ATO NGs. f) Magnified high-resolution XPS spectra of IrO_2@BSA-ATO NGs. g) UV–vis spectra of ATO, IrO_2@BSA, and IrO_2@BSA-ATO NGs. h) FT-IR spectra of ATO, IrO_2@BSA, and IrO_2@BSA-ATO NGs. i) Thermogravimetric analysis of IrO_2@BSA and IrO_2@BSA-ATO NGs.

dynamic light scattering (DLS). As anticipated, successful ATO loading is corroborated by an increase in the average hydrodynamic diameter from 30.73 nm to 56.37 nm, as well as a shift in the zeta potential from −32.58 mV to −42.81 mV (Fig. 1D). The discrepancy between the size obtained by DLS and previous TEM could be ascribed to the fact that DLS measures a hydrodynamic diameter based on the NG diffusion coefficient, and thus it also takes into account the hydration layer surrounding the particles. Peaks corresponding to C 1s, O 1s, and Ir 4f are observed in the X-ray photoelectron spectroscopy (XPS) survey scan of $IrO_2@BSA$-ATO NGs powder (Fig. 1E). Furthermore, the high-resolution XPS spectra of Ir 4f (Fig. 1F) exhibit characteristic peaks at 61.8 eV and 64.6 eV, assignable to 4f 7/2 and 4f 5/2 of Ir^{4+} [34]. Therefore, Ir species in the NGs exist mainly in a tetravalent oxidation state. Although the X-ray diffractogram lacks discernible peaks, it aligns with the standard peak of IrO_2 (JCPDS 15–0870) (Fig. S1) [35]. In the UV–vis absorption spectrum, the dispersed $IrO_2@BSA$-ATO NGs exhibited a broad peak at approximately 430 nm, which could be attributed to the successful loading of ATO (Fig. 1G). Fourier Transform Infrared Spectroscopy (FTIR) reveals characteristic absorption bands corresponding to amide I and amide II at $\sim$1656 cm^{-1} and $\sim$1568 cm^{-1} aligning with BSA

scaffolds of $IrO_2@BSA$-ATO NGs (Fig. 1H). Additionally, a distinct peak at $\sim$3373 cm^{-1} is observed, attributed to the migration of the signature infrared peak of pristine ATO. To determine the ATO loading content within the $IrO_2@BSA$-ATO NGs, a thermalgravimetric analysis (TGA) curve was obtained. Comparing the TGA curves for $IrO_2@BSA$ and $IrO_2@BSA$-ATO elucidates that the ATO percentage in $IrO_2@BSA$-ATO NGs is approximately 5.51 % (w/w) (Fig. 1I). Taken together, these results demonstrated that the bioinspired ultrasmall $IrO_2@BSA$-ATO NGs were successfully synthesized.

## 2.2. Photothermal effects, oxygen generation and photodynamic property in vitro

The $IrO_2@BSA$-ATO NGs demonstrate a robust NIR absorbance, a pivotal attribute for the PA imaging-guided PTT in one platform [36]. And the absorption intensity of $IrO_2@BSA$ NPs at 808 nm is linearly dependent on the concentration (Fig. S4), which could be consistent with the satisfactory PA and PTT behavior. As expected, the results in Fig. 2A depicted a discernible augmentation in PA signal intensities corresponding to the increasing $IrO_2@BSA$-ATO NGs concentrations,
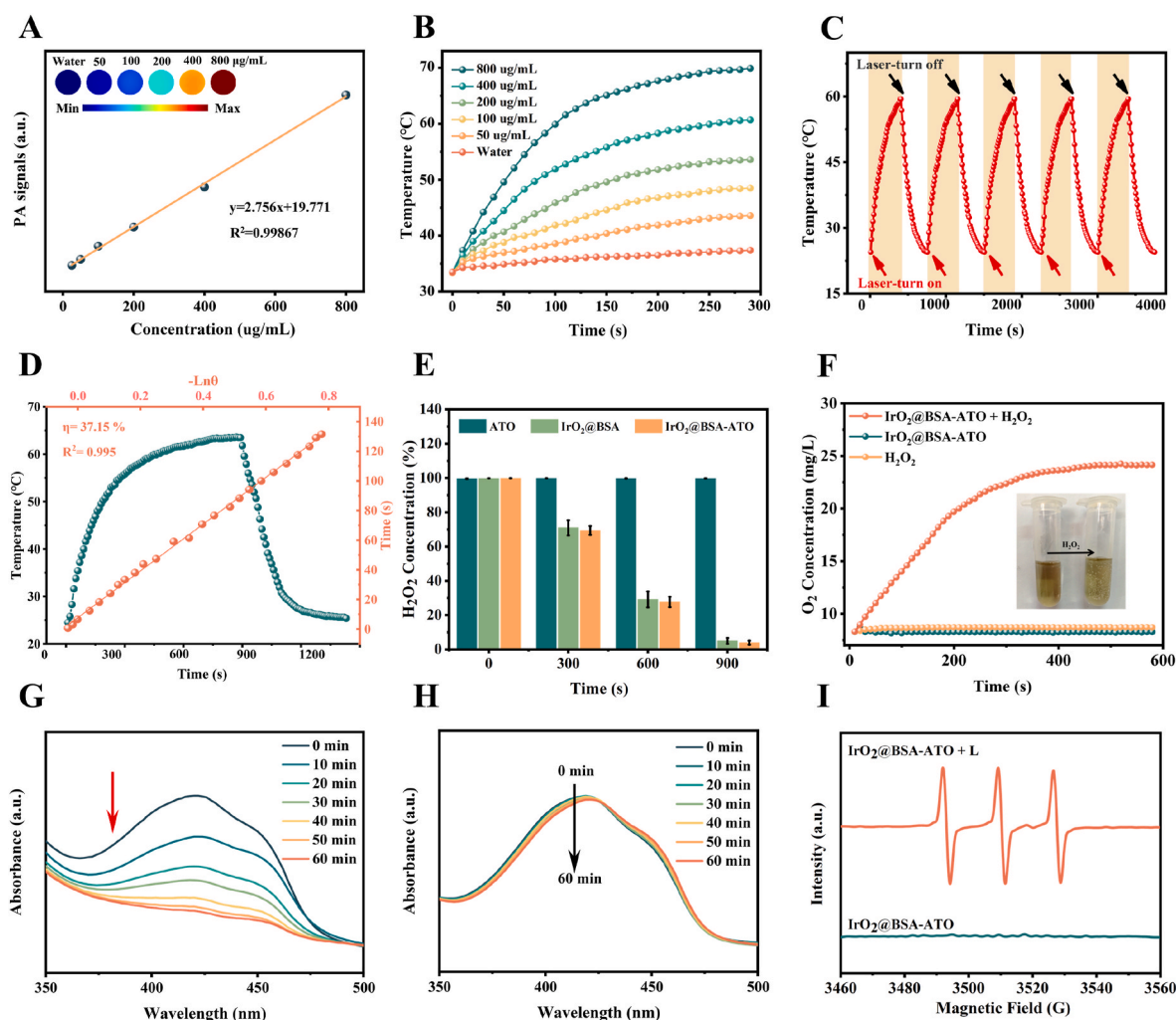
Fig. 2. Photothermal effects, oxygen generation and photodynamic property *in vitro*. a) PA images and PA signals of $IrO_2@BSA$-ATO NGs aqueous solutions at different concentrations b) Concentration-dependent photothermal curves of $IrO_2@BSA$-ATO NGs aqueous solutions Photothermal effect of $IrO_2@BSA$-ATO NGs with different concentrations upon 5 min of irradiation (808 nm, 1.0 W/cm^2). c) Photothermal stability of $IrO_2@BSA$-ATO NGs (400 μg/mL) under five heating-cooling cycles (808 nm, 1.0 W/cm^2). d) Photothermal conversion efficiency of $IrO_2@BSA$-ATO NGs. e) *In vitro* decomposition behavior of H_2O_2 after incubation with ATO, $IrO_2@BSA$, and $IrO_2@BSA$-ATO NGs. f) H_2O_2-decomposition triggered O_2 generation curves of ATO, $IrO_2@BSA$, and $IrO_2@BSA$-ATO NGs. g) The UV spectra of time-dependent DPBF degradation after incubated with $IrO_2@BSA$-ATO NGs (100 μg/mL) under 808 nm irradiation (1.0 W/cm^2). h) UV spectra of DPBF before and after incubated with $IrO_2@BSA$-ATO NGs (100 μg/mL) for 60min without irradiation. i) ESR spectra of TEMP in the presence of $IrO_2@BSA$-ATO NGs with and without laser irradiation.

and a linear relationship between PA signal intensity and IrO$_2$@B-SA-ATO NGs concentration was established. PTT is a well-known non-invasive strategy for tumor ablation by converting light energy into heat, with minimal damage to surrounding normal cells [37]. To systematically assess the photothermal conversion efficacy of the NGs, temperature increments were monitored by subjecting aqueous NGs solutions to various concentrations under an 808 nm laser at 1W/cm^2. It was found that the dispersion of IrO$_2$@BSA-ATO NGs displays a

concentration-dependent temperature increase when exposed to laser radiation (Fig. 2B). Specifically, the IrO$_2$@BSA-ATO group (400 μg/mL) exhibited a substantial temperature increase from 23.5 °C to 50.7 °C within 5 min of irradiation (sufficient for hyperthermic killing of tumor cells), while negligible temperature fluctuations (<5 °C) were observed in the control group. Upon multiple on-off cycles of laser exposure (five times), the maximum temperature rise remained consistently unchanged, attesting to the commendable reproducibility and stability of
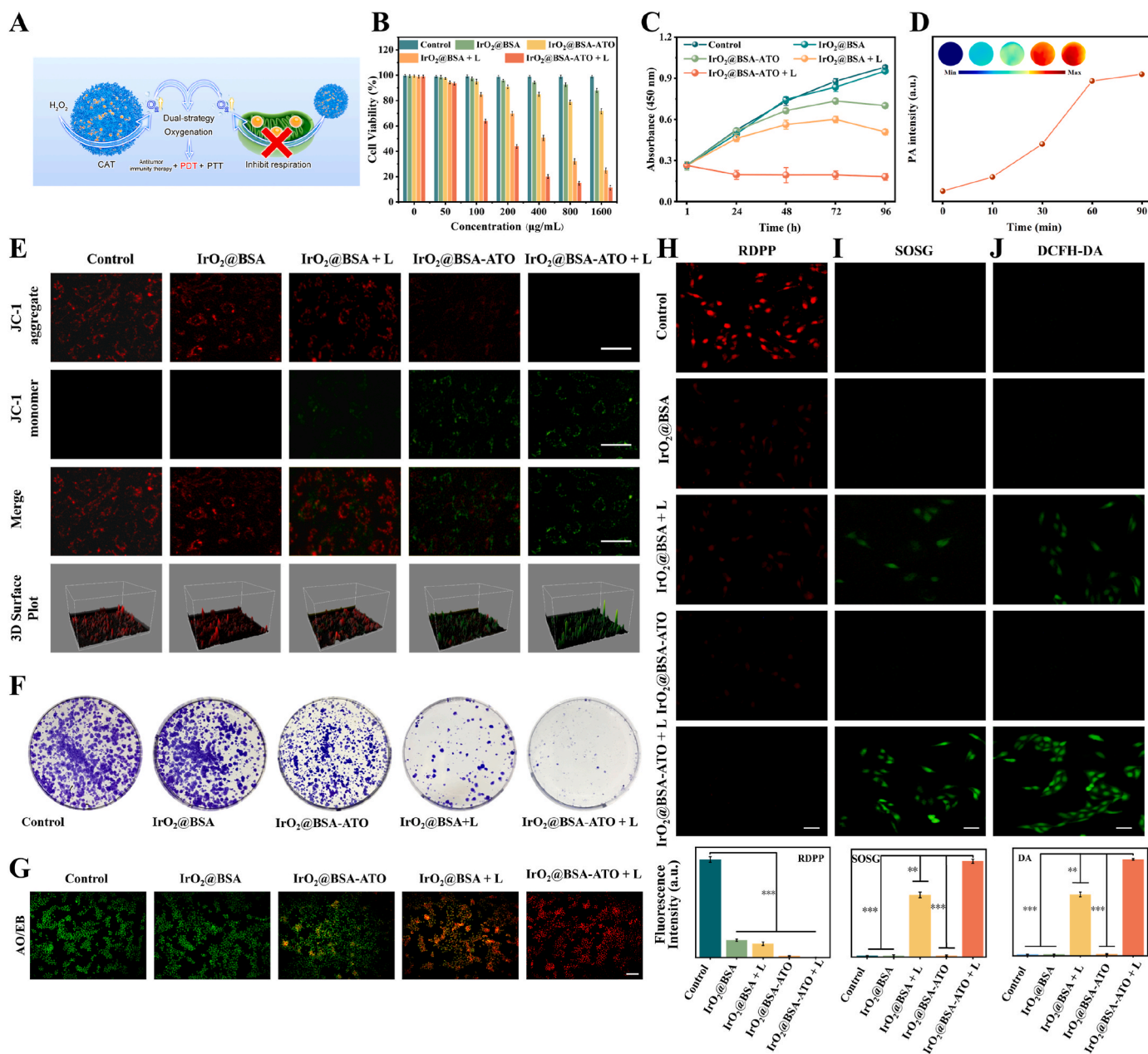
Fig. 3. PA cellular uptake and multi-therapeutic effects at the cellular level. a) Schematic illustration of the dual-strategy for increasing tumor oxygenation, which ultimately enhanced PDT efficacy. b) The viability of LM8 cells after incubation with IrO$_2$@BSA, IrO$_2$@BSA-ATO NGs at different concentrations with or without laser irradiation (808 nm, 1 W/cm^2). c) The growth curves of LM8 cells were subjected to different treatments using standard CCK-8 assay over a period of four days. d) Averaged photoacoustic signal intensity of cell suspension in phantom regions according to cellular uptake time. e) JC-1 staining of LM8 cells after diverse treatments: (1) control, (2) IrO$_2$@BSA, (3) IrO$_2$@BSA + 808 nm laser, (4) IrO$_2$@BSA-ATO NGs, (5) IrO$_2$@BSA-ATO NGs + 808 nm laser. The red JC-1 for normal membrane potential mitochondria, and the green JC-1 monomer for depolarized membrane mitochondria (scale bar = 50 μm). f) Colony formation was detected by single-cell clone assay g) AO/EB staining images of LM8 cells after diverse treatments. Scale bars: 100 μm. h) RDPP probe detecting intracellular oxygen generation level of LM8 after different treatments. Scale bar, 50 μm. i, j) Evaluation of intracellular ROS generation with DCFH-DA (intracellular ROS probe) and singlet oxygen sensor green (SOSG). Scale bar, 50 μm. Laser irradiation, 1 W/cm^2, 10 min n = 5. Corresponding quantitative data of each staining are presented below the representative pictures. Mean ± SD (n = 3). *P < 0.05, **P < 0.01, ***P < 0.001. (For interpretation of the references to color in this figure legend, the reader is referred to the Web version of this article.)

the NGs (Fig. 2C). The calculated photothermal conversion efficiency of the NGs approximates 37.15 % (Fig. 2D), consistent with previously reported values for IrO_2-based Photothermal Agents (PTAs), affirming the proficiency of IrO_2@BSA-ATO NGs as formidable contributors to the field of PTT. These results have demonstrated the potential of IrO_2@BSA-ATO NGs for precise PA imaging-guided PTT *in vivo*.

Catalase (CAT) serves as a catalyst for the degradation of hydrogen peroxide (H_2O_2) into oxygen (O_2) and water [38]. The CAT activity of IrO_2@BSA-ATO NGs was gauged by monitoring the reduction in H_2O_2 consumption and the concurrent increase in O_2 production. Fig. 2E vividly illustrates a substantial reduction in H_2O_2 concentration in both the IrO_2@BSA and IrO_2@BSA-ATO groups when compared to the pure ATO group. Additionally, this reduction was accompanied with an elevation of O_2 concentration over time, as determined by a portable dissolved oxygen meter (Fig. 2F). The visually apparent appearance of bubbles intuitively signifies the generation of O_2 in the tumor-like microenvironment (the inset in Fig. 2F). This in situ production of O_2 serves as an effective means to bolster intracellular O_2 concentration, a strategic "broadening sources" approach that augments the oxygenation milieu, thereby enhancing the efficacy of photodynamic therapy (PDT).

With regard to PDT, the effect hinges upon the capacity of photosensitizers (PS) to channel energy from lasers to tumor-dissolved O_2, instigating the generation of cytotoxic singlet oxygen ($^1O_2$) for tumor treatment. The absorption of DPBF at the wavelength of 410 nm, inversely linked to the production of $^1O_2$, stands as a dependable indicator of the reaction process. Fig. 2G depicts a gradual decline in the absorption intensity of DPBF with increasing irradiation time during NIR laser exposure, attesting to the sustained production of $^1O_2$ and the commendable photodynamic efficacy of the NGs. In contrast, the characteristic peak without laser irradiation exhibited no discernible decrease (Fig. 2H). Furthermore, using 2,2,6,6-tetramethylpiperidine (TEMP) as a specific $^1O_2$ trapping agent, a robust triplet signal with an intensity ratio of 1:1:1, corresponding to TEMPO, was detected after laser irradiation, unequivocally confirming the formation of $^1O_2$ (Fig. 2I). Collectively, the multifunctional IrO_2@BSA-ATO NGs demonstrate a dual prowess, concurrently exhibiting PDT and CAT-like activity. This dual functionality facilitates the production of O_2 for augmenting PDT-induced highly toxic $^1O_2$ production, thereby fostering efficient tumor cells apoptosis.

2.3. PA cellular uptake and multi-therapeutic effects at the cellular level

Buoyed by the exceptional characteristics exhibited by IrO_2@BSA-ATO NGs thus far, we delved deeper into their intracellular hypoxia relief, ROS generation, as well as the antitumor efficacy. The innovative dual-strategy of IrO_2@BSA-ATO NGs for addressing the hypoxia dilemma, could ultimately amplify the intracellular ROS generation from PDT, and eradicate tumor cells, as illustrated in Fig. 3A. For antitumor efficacy, the cytotoxicity of the NGs towards LM8 cells was initially assessed utilizing a CCK-8 assay (Fig. 3B). In the IrO_2@BSA group, the cell viability of LM8 cells shows no obvious changes even at a high concentration of 800 μg/mL, suggesting excellent cytocompatibility, which should be the first consideration for clinical applications. In stark contrast, the IrO_2@BSA-ATO NGs + Laser group emerged with the most promising outcome in terms of cytotoxicity. For example, under the irradiation of NIR, the cell viability was below 20 % when co-incubated with 400 μg/mL NGs. Fig. 3C portrays a time-dependent inhibition of cell proliferation in LM8 cells treated with IrO_2@BSA-ATO NGs + Laser, spanning from 24 to 96 h. It was found that no substantial inhibitory effect was observed in cells treated with the negative control. However, in the IrO_2@BSA-ATO NGs + Laser group, cell proliferation was completely inhibited. Following co-incubation with IrO_2@BSA-ATO NGs for varying durations, the harvested cells were scrutinized for PA intensity. Remarkably, the PA signal of the cell suspension in the phantom manifested within 10 min, reaching its zenith in 90 min (Fig. 3D). This temporal pattern mirrors the process of cellular

internalization, serving as an indirect reflection of the NGs' entry into the cellular milieu. The assessment of photoacoustic cell uptake efficiency lays a pivotal foundation for the subsequent *in vivo* PA imaging of IrO_2@BSA-ATO NGs.

Following the NGs internalization by cells, the ATO molecule competitively inhibits mitochondrial oxidative phosphorylation, precipitating a reduction in mitochondrial membrane potential (MMP) and O_2 consumption. Therefore, inhibition of mitochondrial oxidative phosphorylation of cells after treatment with IrO_2@BSA-ATO NGs can be indirectly determined through mitochondrial functional change. The evaluation of mitochondrial function under various treatments employed a cyanine dye, JC-1, to gauge MMP. As anticipated, groups devoid of ATO exhibited heightened MMP, as indicated by the prevalent population of red fluorescence (J-aggregate). In contrast, ATO-containing treatment groups showcased a profusion of green fluorescence (J-monomer), indicative of a depolarized mitochondrial membrane (Fig. 3E). The effective inhibition of tumor cell respiratory activity resulted in a reduction of the oxygen consumption rate (OCR), constituting a strategic "reducing expenditure" approach to oxygenation. This reduction strategically amplifies the efficacy of PDT synergistically.

We extended our investigation to directly assess the efficacy of the dual strategy of simultaneous oxygen conservation and generation, aiming to enhance intratumoral oxygen tension *in vitro*. Intracellular O_2 content was examined using a conventional oxygen probe, [Ru(dpp)$_3$]Cl$_2$ (RDPP), which exhibits fluorescence quenching in the presence of O_2 [39]. Compared to the hypoxic control group, LM8 cells treated with IrO_2@BSA and IrO_2@BSA + Laser groups exhibited a diminished red fluorescence signal, attributed to the O_2 supplement facilitated by the CAT activity of IrO_2@BSA. Notably, the IrO_2@BSA-ATO ± Laser groups displayed the weakest red fluorescence signals, underscoring the effectiveness of this dual-strategy in augmenting intracellular O_2 concentrations *in vitro* (Fig. 3H). Furthermore, the intracellular generation of $^1O_2$ after enhanced PDT treatment was assessed using a fluorescent singlet oxygen sensor green (SOSG) probe. After laser irradiation, LM8 cells treated with IrO_2@BSA-ATO exhibited stronger green fluorescence than those treated with IrO_2@BSA, while the remaining groups displayed no visible fluorescence (Fig. 3I). This observation implies a higher generation of $^1O_2$ by IrO_2@BSA-ATO NGs *in vitro*. To monitor the generation of reactive oxygen species (ROS), the oxidant-sensitive fluorescent probe 2,7-dichlorodihydrofluorescein diacetate (DCFH-DA) was employed. As anticipated, the efficient generation of ROS under laser irradiation aligned with intracellular $^1O_2$ production (Fig. 3I). The quantitative data of RDPP, SOSG, and DCFH-DA fluorescence staining were consistent with the findings observed in the representative fluorescent microscopic images. These results unequivocally affirm that IrO_2@BSA-ATO NGs possess superior efficacy in improving tumor oxygenation and enhancing PDT *in vitro*.

The therapeutic impact on tumors can be significantly enhanced by amalgamating enhanced PDT with synchronized photothermal therapy under a single laser. The results of the colony formation assay further underscored reduced colony formation and heightened therapeutic efficacy in the IrO_2@BSA-ATO + Laser group (Fig. 3F), aligning with the earlier findings of the CCK-8 assay. To intuitively assess the therapy efficacy of NGs, LM8 cells were doubly stained using acridine orange-ethidium bromide (AOEB), capable of distinguishing between living cells (green) and dead cells (red). Under laser irradiation, almost all cells in the IrO_2@BSA-ATO group were eradicated, showcasing a markedly stronger therapeutic effect compared to other groups (Fig. 3G).

2.4. In vivo PA imaging and ex vivo biodistribution

Given their favorable size and *in vitro* photoacoustic performance, IrO_2@BSA-ATO NGs are anticipated to serve as an outstanding contrast agent for real-time PA imaging *in vivo*. To assess the targeting and monitoring ability of IrO_2@BSA-ATO NGs *in vivo* tumors, mice bearing subcutaneously implanted LM8 tumors were intravenously administered

NGs solution (10 mg/kg) via tail vein injection and scanned at various time points after injection. Following injection, PA signals in tumor regions gradually increased, reaching their zenith at 10 h post-injection (Fig. 4A), implying the passive targeting of IrO$_2$@BSA-ATO NGs in solid tumors, which is likely through the enhanced permeability and retention (EPR) effect due to their suitable size and biocompatibility. Subsequent analysis of the quantitative PA signal revealed a ratio of 16.6 between 10 h post-injection and pre-injection, consistent with the PA images (Fig. 4B). Notably, robust PA signals were distinctly detected throughout the tumor regions, signifying the deep penetration and uniform distribution of IrO$_2$@BSA-ATO NGs in the tumor.

Accumulation of IrO$_2$@BSA-ATO NGs in tumor sites could elevate oxygen concentration by the dual strategy, alleviating hypoxia and enhancing the efficiency of PDT. To evaluate the extent of tumor oxygenation before and after treatment, photoacoustic imaging was employed to differentiate areas of oxyhemoglobin (HbO$_2$, red) and deoxyhemoglobin (Hb, blue). As predicted, the PA signal of HbO$_2$ noticeably increased 12 h after injection, while the intensity of the Hb signal exhibited an opposite trend (Fig. 4C). Quantitative analysis of photoacoustic images corroborated this pattern of elevated oxygenation within the tumor (Fig. 4D). The changes in HbO$_2$ and Hb concentrations *in vivo* revealed that the oxygen nanogenerators could effectively control O$_2$ consumption and increase O$_2$ content at the tumor regions, which was beneficial for the subsequent more efficient PDT. The biodistribution of IrO$_2$@BSA-ATO NGs was further elucidated by quantifying the Ir content in major organs and tumors using inductively coupled plasma mass spectrometry (ICP-MS). Progressive accumulation in the tumor regions over 10 h (10.48 % ID/g) was observed, further indicating the tumor enrichment ability of IrO$_2$@BSA-ATO NGs (Fig. 4E). A substantial amount of NGs accumulated in the liver and spleen, consistent with their role as primary organs of the reticuloendothelial system. *In vivo* PA imaging and ex vivo biodistribution collectively demonstrated efficient tumor-targeted accumulation of IrO$_2$@BSA-ATO NGs, significantly increasing tumor oxygenation by

dual strategy. Accordingly, IrO$_2$@BSA-ATO NGs served as excellent photoacoustic (PA) imaging contrast agents, enabling the simultaneous monitoring and precise guidance of tumor synergy therapy.
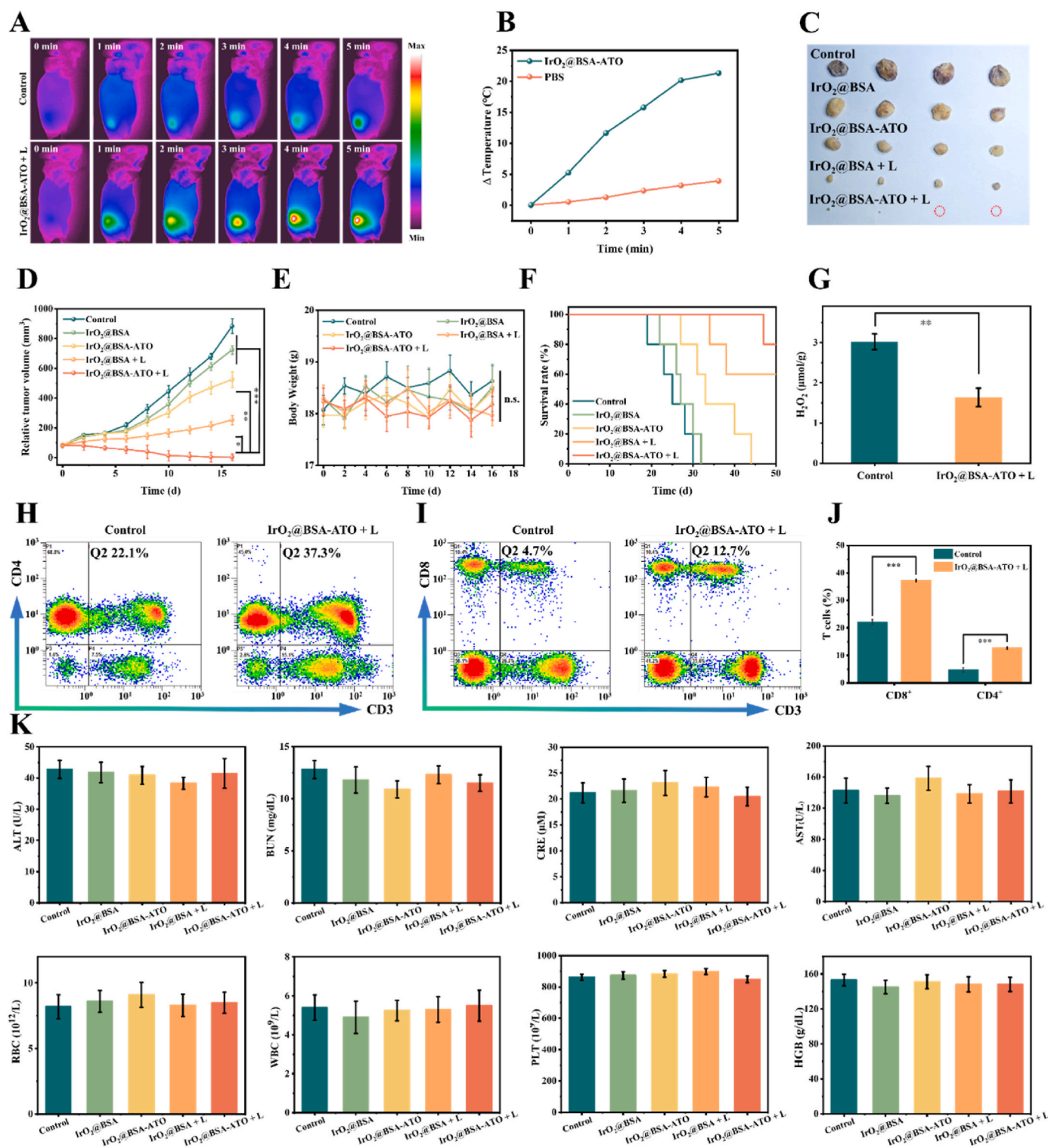
2.5. In vivo antitumor study

Moving to the *in vitro* therapeutic assessment of IrO$_2$@BSA-ATO NGs in LM8 tumor-bearing C3H mice, the evaluation began with an examination of the PTT effect. Mice were randomly divided into two groups, and 5 min of NIR irradiation was administered **10 h** after intravenous injection of PBS and IrO$_2$@BSA-ATO NGs solution, respectively. Temperature changes at the tumor sites were monitored using an infrared camera during the irradiation process (Fig. 5A). In the IrO$_2$@BSA-ATO NGs group, the temperature at the tumor site heated up rapidly and ultimately increased by approximately 21.3 °C after 5 min of irradiation (Fig. 5B). This temperature alteration was sufficient to induce cell death in the tumor. In marked contrast, no obvious temperature change was observed in the control group that received PBS after the NIR irradiation at the same time. The elevated temperature in the tumor regions of the NGs group could be attributed to efficient accumulation by the EPR effect, aligning with the *in vivo* distribution results.

Considering the enhanced PDT ability observed *in vitro*, it is reasonable to assume that NGs can induce the PDT effect *in vivo* under single NIR laser irradiation. Besides, robust PDT as well as PTT can not only directly kill tumor cells but also induce immunogenic cell death (ICD), providing antitumor immunity and long-term immunological memory [40]. In light of this scenario, the antitumor efficiency of PA imaging-guided triple therapy (enhanced-PDT, PTT, and induced antitumor immunity therapy) were investigated in LM8 tumor-bearing mice. Next, the anti-tumor effects by IrO$_2$@BSA-ATO NGs with or without NIR irradiation (808 nm, 1.0 W/cm^2, 5 min) was studied by monitoring the tumor volume every two days over the entire course of treatment. The LM8 tumor-bearing C3H mice with a tumor size of 80–100 mm^3 were randomly divided into five groups for different treatments: (1) PBS, (2)
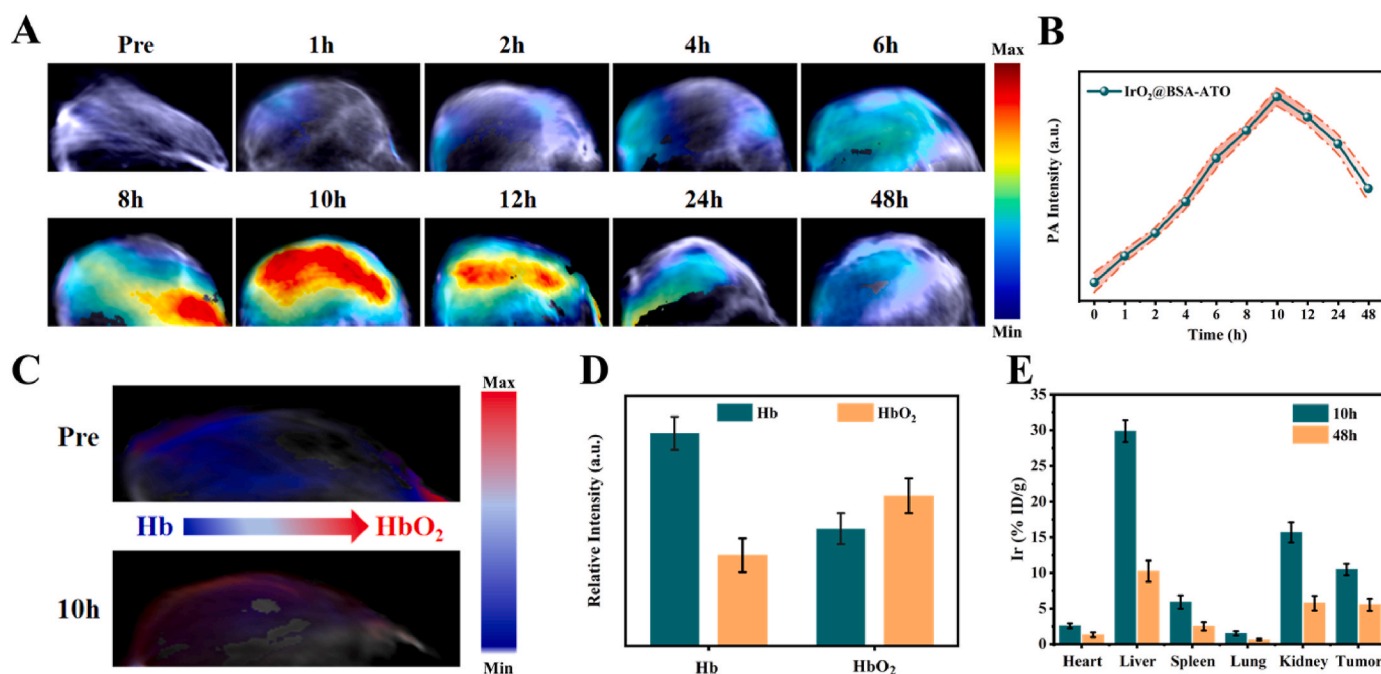
Fig. 4. In vivo PA imaging and ex vivo biodistribution. a) *In vivo* PA images of the LM8 tumor-bearing mice before and after i.v. injection with IrO$_2$@BSA-ATO NGs at the dose of 15 mg/kg during 48 h post-injection under 808 nm laser irradiation (0.3 W/cm2). b) Semi-quantitative analysis of PA signals from tumor regions at various times. c) Representative PA images before and after treatment at tumor regions denoting deoxyhemoglobin (Hb) on the blue color scale and oxyhemoglobin (HbO$_2$) on the red color scale. d) Semi-quantitative analysis of tumor oxygenation extracted from PA images. e) Long-term biodistribution of IrO$_2$@BSA-ATO NGs tumors and main organs of the mice after i.v. injection. Mean ± SD (n = 3). *P < 0.05, **P < 0.01, ***P < 0.001. (For interpretation of the references to color in this figure legend, the reader is referred to the Web version of this article.)

Fig. 5. *In vivo* antitumor study. a) Infrared thermal images and b) the corresponding tumor temperature curves of PBS and IrO$_2$@BSA-ATO NGs against time under NIR laser irradiation (808 nm, 1 W/cm^2). c) Representative digital images of the tumors. d) tumor growth curves, and e) relative body weight of the mice from different groups after treatments. (n = 5) f) Percent survival of the mice. (n = 5). g) H$_2$O$_2$ concentration of excised tumor tissue homogenates of control and IrO$_2$@BSA-ATO NGs + Laser group by the micro plate method. h, i) Representative flow cytometric analysis of the tumor-infiltrated CD4$^+$ T cells and CD8$^+$ T cells. j) Quantitation of the percent of CD4$^+$ T cells and CD8$^+$ T cells in the tumor treated with IrO$_2$@BSA-ATO NGs + Laser group and PBS group. k) Routine blood tests and blood biochemistry. Mean ± SD (n = 5). *P < 0.05, **P < 0.01, ***P < 0.001.

IrO$_2$@BSA, (3) IrO$_2$@BSA-ATO NGs, (4) IrO$_2$@BSA + Laser, and (5) IrO$_2$@BSA-ATO NGs + Laser.

Tumor tissue after the period (16 d) of different treatments is shown in Fig. 5C, where the growth of tumors in the IrO$_2$@BSA-ATO NGs +

Laser group dramatically regressed and even eliminated over time, indicating high synergistic therapy efficiency. Tumor volumes were measured and calculated every 2 days (Fig. 5D). In comparison to both the laser group and the control group, tumor growth in the IrO$_2$@BSA-

ATO NGs + Laser group was predominantly inhibited or even eliminated after 16 d of treatment. Throughout the treatment period (16 d), mice from various groups exhibited no apparent changes in body weight (Fig. 5E), indicating minimal adverse effects. The survival curves of mice revealed that the IrO$_2$@BSA-ATO NGs + Laser group significantly inhibited tumor growth and displayed a high survival rate (80 %) after 50 d. A survival rate of 60 % after 50 d was seen in the group receiving IrO$_2$@BSA + Laser treatment, while mice in the other groups succumbed within 19–44 days (Fig. 5F).

The remarkable inhibition effects on tumors observed with IrO$_2$@BSA-ATO NGs can be attributed to the successful implementation of the dual-strategy to alleviate hypoxia, providing an additional O$_2$ source for PDT, and the favorable induced antitumor immunity performance *in vivo*. Initially, to validate the exogenous O$_2$ production in tumors triggered by the CAT activity of NGs, H$_2$O$_2$ concentrations in fresh tumor tissue homogenates treated with NGs and PBS were measured using an H$_2$O$_2$ detection kit. After intravenous injection of IrO$_2$@BSA-ATO NGs, the H$_2$O$_2$ levels in the tumor tissue homogenates were significantly reduced and notably lower than those after treatment with PBS (3.02 μmol/g versus. 1.63 μmol/g) (Fig. 5G). As mentioned earlier, enhanced PDT and synergetic PTT can release tumor-associated antigens (TAAs), stimulating the activation and proliferation of antitumor T cells. To be specific, when naive T cells are exposed to appropriate antigenic and co-stimulatory cues, they initiate clonal expansion and differentiate into effector cells, resulting in a substantial increase in the number of cells. In this study, we investigated whether enhanced PDT could trigger an antitumor immune response using an LM8 tumor-bearing model. Compared with the PBS group, obvious T cell proliferation was observed in the IrO$_2$@BSA-ATO NGs + Laser group (Fig. 5H and I). Furthermore, CD8$^+$ T cells divide faster and exhibit a greater clonal expansion level compared to CD4$^+$ T cell subsets (Fig. 5J), which can directly eliminate tumor cells by recognizing specific antigens [41]. In the IrO$_2$@BSA-ATO NGs + Laser group, the proportion of CD8$^+$ and CD4$^+$ T cells increased to 12.7 % and 37.3 %, respectively, which was about 2.7 and 1.7 times that in the control group (4.7 % and 22.1 %). Overall, tumor cells treated by enhanced PDT and synergistic PTT can improve the proliferation and activation of T cells in situ (especially CD8$^+$ T cells), and can be employed for the effective therapy of tumors.

After different treatments, mice were subjected to whole blood routines and typical physiochemistry tests in serum to verify the biological safety. The results revealed no statistical differences between the IrO$_2$@BSA-ATO NGs + Laser group and mice treated with PBS in all examined parameters, confirming that IrO$_2$@BSA-ATO NGs have no significant renal or hepatic toxicity (Fig. 5K). In addition, major organs of the mice (heart, liver, spleen, lung, and kidney) in each group were collected for H&E staining, and the results demonstrated no obvious organ damage in all groups (Fig. S2), suggesting the negligible toxic side effects of IrO$_2$@BSA-ATO NGs *in vivo*.

Meanwhile, the biocompatibility character of the NGs was evaluated *in vitro* with a hemolytic assay. The results of the hemolytic activities in Fig. S3 showed that no obvious hemolysis effect appears, and the hemolysis ratio of NGs at all concentrations (0–800 μg/mL) is less than 5 %, which ensures blood safety for clinical usage. In conclusion, these results demonstrated that IrO$_2$@BSA-ATO NGs exhibit excellent biosafety and a commendable synergistic effect of synergistic photodynamic-photothermal-induced antitumor immunity therapy *in vivo*, showing great potential for tumor therapy.

3. Conclusion

In conclusion, we designed a dual-strategy of "reducing expenditure of O$_2$ and broadening sources" to systematically increase tumor oxygenation in osteosarcoma (OS) to boost PDT efficacy, which is achieved by integrating cell respiration inhibitor atovaquone (ATO) into oxygen nanogenerators (NGs) via a facile synthesis procedure. Our results demonstrated that, after the maximum aggregation of IrO$_2$@BSA-

ATO NGs in tumor at 10 h post-injection, as has been proven both *in vivo* and ex vivo, tumor oxygenation can be bilaterally enhanced by the CAT-mimicking activity of the NGs inherently and the respiratory inhibition from released ATO. Furthermore, the anti-hypoxia activities of the bioinspired IrO$_2$@BSA-ATO NGs were demonstrated by the increased O$_2$ content *in vitro* and enhanced PA signal of HbO$_2$ *in vivo*, resulting in a marked enhancement of the PDT effect. Systematic studies have revealed that, triggered by a single NIR laser, these multifunctional NGs present a great prospect for photoacoustic imaging (PAI)-guided photothermal therapy (PTT) and elicit a notable synergistic effect with induced antitumor immunotherapy simultaneously. In summary, a unique binary oxygen nanogenerator was rationally designed to overcome the hypoxia barrier in PDT, which in turn enabled OS synergetic PDT/PTT/induced antitumor immunity therapy, exhibiting great potential for precise PA imaging-guided three-in-one therapeutic effects.

Experimental section

Methods and any associated references are available in the Supporting Information.

CRediT authorship contribution statement

Chongqing Zhang: Writing – original draft, Data curation, Conceptualization. **Dongsheng Li:** Writing – review & editing, Visualization, Data curation. **Xin Zhang:** Investigation, Formal analysis, Data curation. **Rong Dai:** Investigation, Data curation. **Weiwei Kang:** Software, Methodology, Formal analysis. **Yao Li:** Methodology, Investigation, Data curation. **Qin Liu:** Methodology, Investigation, Data curation. **Mengting Gao:** Software, Methodology, Data curation. **Ziliang Zheng:** Writing – review & editing, Investigation, Funding acquisition, Conceptualization. **Ruiping Zhang:** Supervision, Project administration, Funding acquisition. **Zhaohui Wen:** Supervision, Project administration, Funding acquisition.

Declaration of competing interest

The authors declare that they have no known competing financial interests or personal relationships that could have appeared to influence the work reported in this paper.

Data availability

The authors do not have permission to share data.

Acknowledgments

Appendix A. Supplementary data

Supplementary data to this article can be found online at https://doi. org/10.1016/j.mtbio.2024.101054.

References

[1] W. Chen, Z. Li, N. Yu, L. Zhang, H. Li, Y. Chen, F. Gong, W. Lin, X. He, S. Wang, J. Nanobiotechnol. 21 (1) (2023) 355.

[2] G. Wei, T. Zhang, Z. Li, N. Yu, X. Xue, D. Zhou, Y. Chen, L. Zhang, X. Yao, G. Ji, Aging (N. Y.) 12 (7) (2020) 6172.

[3] A.M. Czarnecka, K. Synoradzki, W. Firlej, E. Bartnik, P. Sobczuk, M. Fiedorowicz, P. Grieb, P. Rutkowski, Cancers 12 (8) (2020) 2130.

[4] X. Zhao, Q. Wu, X. Gong, J. Liu, Y. Ma, Biomed. Eng. 20 (2021) 1–14.

[5] A. Smrke, P.M. Anderson, A. Gulia, S. Gennatas, P.H. Huang, R.L. Jones, Cells 10 (1) (2021) 172.

[6] J. Lv, S. Wang, D. Qiao, Y. Lin, S. Hu, M. Li, J. Nanobiotechnol. 20 (1) (2022) 1–16.

[7] J. Xie, Y. Wang, W. Choi, P. Jangili, Y. Ge, Y. Xu, J. Kang, L. Liu, B. Zhang, Z. Xie, Chem. Soc. Rev. 50 (16) (2021) 9152–9201.

[8] Y. Wang, S. Fu, Y. Lu, R. Lai, Z. Liu, W. Luo, Y. Xu, Carbohydr. Polym. 277 (2022) 118819.

[9] K. Khorsandi, R. Hosseinzadeh, H. Esfahani, K. Zandsalimi, F.K. Shahidi, H. Abrahamse, Inflamm. Regen. 42 (1) (2022) 1–20.

[10] J. Liu, X. Zhao, W. Nie, Y. Yang, C. Wu, W. Liu, K. Zhang, Z. Zhang, J. Shi, Theranostics 11 (1) (2021) 379.

[11] T.B. Thapa Magar, J. Lee, J.H. Lee, J. Jeon, P. Gurung, J. Lim, Y.-W. Kim, Pharmaceutics 15 (6) (2023) 1577.

[12] D. Shakiba, G.M. Genin, S.P. Zustiak, Adv. Drug Deliv. Rev. (2023) 114771.

[13] Y. Xiong, Z. Yong, C. Xu, Q. Deng, Q. Wang, S. Li, C. Wang, Z. Zhang, X. Yang, Z. Li, Adv. Sci. (2023) 2301278.

[14] J. Wang, J. Sun, W. Hu, Y. Wang, T. Chou, B. Zhang, Q. Zhang, L. Ren, H. Wang, Adv. Mater. 32 (22) (2020) 2001862.

[15] M. Li, Y. Xu, X. Peng, J.S. Kim, Acc. Chem. Res. 55 (22) (2022) 3253–3264.

[16] X. Li, N. Kwon, T. Guo, Z. Liu, J. Yoon, Angew. Chem., Int. Ed. 57 (36) (2018) 11522–11531.

[17] R.V. Huis, t Veld, J. Heuts, S. Ma, L.J. Cruz, F.A. Ossendorp, M.J. Jager, Pharmaceutics 15 (2) (2023) 330.

[18] J. Wang, B. Zhang, J. Sun, Y. Wang, H. Wang, Adv. Ther. 3 (1) (2020) 1900083.

[19] J. Dai, M. Wu, Q. Wang, S. Ding, X. Dong, L. Xue, Q. Zhu, J. Zhou, F. Xia, S. Wang, Natl. Sci. Rev. 8 (6) (2021) nwab039.

[20] D. Xia, P. Xu, X. Luo, J. Zhu, H. Gu, D. Huo, Y. Hu, Adv. Funct. Mater. 29 (13) (2019) 1807294.

[21] D. García-Sánchez, World J. Stem Cell. 15 (5) (2023) 421.

[22] V. Tragni, G. Primiano, A. Tummolo, L. Cafferati Beltrame, G. La Piana, M. N. Sgobba, M.M. Cavalluzzi, G. Paterno, R. Gorgoglione, M. Volpicella, Molecules 27 (11) (2022) 3494.

[23] G.L. Galli, I.M. Ruhr, J. Crossley, D.A. Crossley, Front. Physiol. 12 (2021) 689684.

[24] Y. Xu, D. Xue, A. Bankhead III, N. Neamati, J. Med. Chem. 63 (23) (2020) 14276–14307.

[25] Y.T. Fan, T.J. Zhou, P.F. Cui, Y.J. He, X. Chang, L. Xing, H.L. Jiang, Adv. Funct. Mater. 29 (10) (2019) 1806708.

[26] C. Ren, X. Xu, D. Yan, M. Gu, J. Zhang, H. Zhang, C. Han, L. Kong, Acta Biomater. 146 (2022) 465–477.

[27] L. Song, B. Chen, Z. Qin, X. Liu, Z. Guo, H. Lou, H. Liu, W. Sun, C. Guo, C. Li, Adv. Healthcare Mater. 11 (8) (2022) 2102298.

[28] H. Wu, Q. Jiang, K. Luo, C. Zhu, M. Xie, S. Wang, Z. Fei, J. Zhao, J. Nanobiotechnol. 19 (2021) 203.

[29] W. Zhen, Y. Liu, L. Lin, J. Bai, X. Jia, H. Tian, X. Jiang, Angew Chem. Int. Ed. Engl. 57 (2018) 10309–10313.

[30] W. Gu, T. Zhang, J. Gao, Y. Wang, D. Li, Z. Zhao, B. Jiang, Z. Dong, H. Liu, Drug Deliv. 26 (2019) 918–927.

[31] D. Yang, Y. Tang, B. Zhu, H. Pang, X. Rong, Y. Gao, F. Du, C. Cheng, L. Qiu, L. Ma, Adv. Sci. (2023) 2206181.

[32] W. Gu, T. Zhang, J. Gao, Y. Wang, D. Li, Z. Zhao, B. Jiang, Z. Dong, H. Liu, Drug Deliv. 26 (1) (2019) 918–927.

[33] Y.-M. Chang, Y.-C. Hsieh, P.-W. Wu, C.-H. Lai, T.-Y. Chang, Mater. Lett. 62 (26) (2008) 4220–4222.

[34] W. Zhen, Y. Liu, L. Lin, J. Bai, X. Jia, H. Tian, X. Jiang, Angew. Chem. 130 (32) (2018) 10466–10470.

[35] D. Li, T. Li, G. Hao, W. Guo, S. Chen, G. Liu, J. Li, Q. Zhao, Chem. Eng. J. 399 (2020) 125738.

[36] X. Yuan, J. Cen, X. Chen, Z. Jia, X. Zhu, Y. Huang, G. Yuan, J. Liu, J. Colloid Interface Sci. 605 (2022) 851–862.

[37] H. Sun, Q. Zhang, J. Li, S. Peng, X. Wang, R. Cai, Nano Today 37 (2021) 101073.

[38] B. Yuan, H.-L. Chou, Y.-K. Peng, ACS Appl. Mater. Interfaces 14 (20) (2021) 22728–22736.

[39] P. Zhang, Y. Shi, Y. Xu, Y. Liang, C. Huang, D. Zhong, Z. Zhang, Y. Yu, Z. Zhang, J. Zhang, Adv. Healthcare Mater. (2023) 2302020.

[40] O. Troitskaya, M. Varlamov, A. Nushtaeva, V. Richter, O. Koval, Molecules 25 (12) (2020) 2804.

[41] A. Cachot, M. Bilous, Y.-C. Liu, X. Li, M. Saillard, M. Cenerenti, G.A. Rockinger, T. Wyss, P. Guillaume, J. Schmidt, Sci. Adv. 7 (9) (2021) eabe3348.